

URANS Study of Air-Layer Drag Reduction in a High-Reynolds-Number Flat-Plate Turbulent Boundary Layer

Zhaoyuan Wang¹, Jianming Yang², Frederick Stern³

IIHR-Hydroscience and Engineering, University of Iowa, Iowa City, IA, 52242-1585, USA

The air layer formation in a high Reynolds-number flat plate turbulent boundary layer is simulated using a two-phase sharp interface Cartesian grid solver. The interface is tracked by a coupled level set and volume-of-fluid method (CLSVOF) and turbulence is modeled by a Spalart-Allmaras (SA) turbulence model with a wall function (WF) approach. The air layer along the entire test plate is successfully achieved and the drag reduction is approximately 100%, which agrees very well with the experimental findings. With reduced air flow rate, bubble drag reduction (BDR) is also observed; the computational results also qualitatively match the experiments. The transitional region from BDR to ALDR is also observed in the present simulation. However, the critical air flow rate to form the ALDR is lower in the simulations than in the experiments. Several possible reasons are likely accounting for the low critical air flow rate in the simulations, such as SA-WF turbulence model, three-dimensional instability and surface tension effects. The critical air flow rate does not change much with grid refinement.

I. Introduction

BUBBLE drag reduction (BDR) is an important technique that injects gas into the liquid turbulent boundary layer to form bubbles to obtain drag reduction. This technique can substantially reduce skin friction, which has great potential applications in ship hydrodynamics. During the past several decades, a large amount of research has been devoted to the BDR.¹ However, most of the studies were conducted at relatively low Reynolds numbers and small scales. Proper scaling of BDR remains unclear.

In the study by Sanders et al.,² a set of BDR experiments were conducted for a large scale flat plate turbulent boundary layer at high Reynolds numbers. It has shown that significant levels of BDR could be achieved only near the air injector, and limited persistence of BDR exists away from the air injector. This short persistence distance of BDR makes it impractical for applications. It has also shown that a layer of gas was formed and persisted along the entire plate at lower flow speeds and higher gas injection rates, which could lead to skin-friction reduction of more than 80%. Elbing et al.³ continued the study of Sanders et al.² in an effort to understand the mechanisms underlying the limited persistence of the BDR and the onset conditions for the air layer drag reduction (ALDR). The experimental results indicated that ALDR could be established once the air was injected beyond a critical rate, and more than 80% drag reduction could be obtained over the entire plate. Three distinct regions associated with drag reduction were observed with air injection rate: BDR, transition and ALDR. It was found that the air layer was sensitive to the inflow conditions. In the recent work,⁴ a 1/2 inch (12.7 mm) step was used at the inlet, and the air was injected from the base of the backward-facing step. This greatly enhances the stability of the air layer. The ALDR is a potential alternative to BDR, however, the knowledge of ALDR mechanism is quite limited and more comprehensive studies are needed. Related to ALDR, partial cavity drag reduction (PCDR) is another important technique to reduce skin friction. PCDR needs potentially lower gas flux compared to ALDR, but un-optimized cavity flow can lead to significant form drag.⁴ Partial cavities are sensitive to flow speed and perturbations from the incoming flow.⁵

In the present study, URANS (unsteady Reynolds-averaged Navier-Stokes) simulations of ALDR on a large scale flat plate are performed. The objective is to validate prediction capability of the computational code, CFDShip-Iowa Version 6.1⁶⁻⁸ for ALDR, investigate the mechanism of ALDR, and explore potential applications to ship hydrodynamics. The simulations are carried out using a sharp interface Cartesian grid solver, with the interface

¹ Assistant Research Scientist, AIAA Member.

² Associated Research Scientist, AIAA Member.

³ Professor of Mechanical Engineering.

tracked by a coupled level set and volume-of-fluid (CLSVOF) method and turbulence modeled by a Spalart-Allmaras (SA) turbulence model⁹ with a wall function (WF) approach. The experimental data reported by Elbing et al.³ is used to validate the simulation results. It is a challenge for the numerical simulation of such flow since high Reynolds numbers, air-water interface, and two-phase turbulence are involved.

II. Mathematical Model and Numerical Methods

A. Navier-Stokes Equations

Incompressible viscous flows of two immiscible fluids, e.g., air and water, are governed by the Navier-Stokes equations:

$$\frac{\partial \mathbf{u}}{\partial t} + \mathbf{u} \cdot \nabla \mathbf{u} = \frac{1}{\rho} \nabla \cdot (-p\mathbf{I} + \mathbf{T}) + \mathbf{g}, \quad (1)$$

$$\nabla \cdot \mathbf{u} = 0, \quad (2)$$

where t is the time, \mathbf{u} is the velocity vector, p is the pressure, \mathbf{I} is the unit diagonal tensor, ρ is the density, \mathbf{g} represents the gravity acceleration, and \mathbf{T} is the viscous stress tensor defined as

$$\mathbf{T} = 2\mu\mathbf{S}, \quad (3)$$

with μ the dynamic viscosity and \mathbf{S} the strain rate

$$\mathbf{S} = \frac{1}{2}(\nabla \mathbf{u} + (\nabla \mathbf{u})^T). \quad (4)$$

Since the fluid properties are discontinuous across the interface, which is a function of time and space, density and viscosity are also functions of time and space and only known with given interface position. Their definitions will be deferred after the introduction of interface representation using the level set function.

B. Turbulence Modeling

In the URANS approach, the turbulent eddy viscosity is obtained by solving a transport equation for an auxiliary variable $\tilde{\nu}$ as proposed by Spalart and Allmaras⁹

$$\frac{\partial \tilde{\nu}}{\partial t} + \mathbf{u} \cdot \nabla \tilde{\nu} = c_{b1} |\tilde{\Omega}| \tilde{\nu} - c_{w1} f_w \left(\frac{\tilde{\nu}}{d}\right)^2 + \frac{1}{\sigma} \left\{ \nabla \cdot [(\nu + \tilde{\nu}) \nabla \tilde{\nu}] + c_{b2} |\nabla \tilde{\nu}|^2 \right\}. \quad (5)$$

The left hand side of the equation consists of the unsteady and advection terms of the turbulent eddy viscosity. The terms of right hand side are the production, destruction and diffusion, respectively. The turbulent eddy viscosity is obtained as

$$\nu_T = f_{v1} \tilde{\nu}, \quad (6)$$

where,

$$f_{v1} = \frac{\chi^3}{\chi^3 + c_{v1}^3}, \quad \chi = \frac{\tilde{\nu}}{\nu}. \quad (7)$$

The production term is based on the magnitude of vorticity,

$$|\tilde{\Omega}| = |\Omega| + \frac{\tilde{\nu}}{\kappa^2 d^2} f_{v2}, \quad |\Omega| = \sqrt{2\Omega \cdot \Omega}, \quad (8)$$

$$\Omega = \frac{1}{2}(\nabla \mathbf{u} - (\nabla \mathbf{u})^T), \quad f_{v2} = 1 - \frac{\chi}{1 + \chi f_{v1}}$$

Mariani and Zilliac¹⁰ provided an improvement to the production term by suppressing the turbulence, i.e., excessive production of eddy viscosity in regions where vorticity magnitude exceeds the strain-rate,

$$|\tilde{\Omega}| = |\Omega| + f \min(0, |\mathbf{S}| - |\Omega|) + \frac{\tilde{\nu}}{\kappa^2 d^2} f_{v2}. \quad (9)$$

They concluded the value of $f \sim 3.5-4.0$ provides best result for wingtip vortex calculations. In present calculations $f = 4.0$ is chosen. The destruction term involves a near-wall damping function which is

$$\begin{aligned}
f_w &= g \left[\frac{1 + c_{w3}^6}{g^6 + c_{w3}^6} \right]^{1/6}, \\
g &= r + c_{w2}(r^6 - r), \\
r &= \frac{\tilde{v}}{|\tilde{\Omega}| \kappa^2 \tilde{d}^2}
\end{aligned} \tag{10}$$

where \tilde{d} is the distance to the nearest wall.

The model constants are

$$\begin{aligned}
c_{b1} &= 0.1355, & c_{b2} &= 0.622, \\
c_{v1} &= 7.1, & \sigma &= 2/3, \\
c_{w1} &= c_{b1} \kappa^{-2} + (1 + c_{b2}) \sigma^{-1} = 3.239, \\
c_{w2} &= 0.3, & c_{w3} &= 2, \\
\kappa &= 0.41, & C_{DES} &= 0.65
\end{aligned} \tag{11}$$

In the multi-phase flows the molecular eddy viscosity is smoothed across the interface using a Heaviside function (refer to Ref. 6) to avoid sharp gradients in molecular viscosity in Eq. (5). In order to capture the effects of viscous boundary layers within the framework of a Cartesian grid solver, a multi-layer wall-function model capable of switching smoothly between *sub*-, *buffer*-, and *log*-layers is used, details are given in the studies.^{8,11}

C. Interface Modeling

Defining the interface Γ as the zero level set of a signed distance function ϕ , or the level set function, the position of the interface can be tracked by solving the level set evolution equation

$$\frac{\partial \phi}{\partial t} + \mathbf{u} \cdot \nabla \phi = 0. \tag{12}$$

To keep ϕ as a signed distance function in the course of the evolution, we iterate the reinitialization equation for the level set function¹²

$$\frac{\partial \phi}{\partial \tau} + S(\phi_o)(|\nabla \phi| - 1) = 0, \tag{13}$$

where τ is the pseudo time and $S(\phi_o)$ is a numerically smeared-out sign function

$$S(\phi_o) = \frac{\phi_o}{\sqrt{\phi_o^2 + h^2}}, \tag{14}$$

with ϕ_o the initial values of ϕ and h a small distance, usually the grid cell size, to smear out the sign function.

In the CLSVOF method, the volume-of-fluid (VOF) function, F , is defined as the liquid volume fraction in a cell with its value in between zero and one in a surface cell and zero and one in air and liquid respectively. The advection equation of F is

$$\frac{\partial F}{\partial t} + \mathbf{u} \cdot \nabla F = 0. \tag{15}$$

The level set function is corrected based on the reconstructed interface using VOF function for mass conservation.

With the level set function defined, the fluid properties, such as density and viscosity, are given by the following equations:

$$\begin{aligned}
\rho &= \rho_G + (\rho_L - \rho_G)F \\
\mu &= \mu_G + (\mu_L - \mu_G)F
\end{aligned} \tag{16}$$

where the subscripts G and L represent gas and liquid phase, respectively.

In terms of jump conditions, the velocity across the interface Γ is continuous, as the fluids are viscous and no phase change is considered here:

$$[\mathbf{u}] = 0, \quad (17)$$

and the jump condition for stress is

$$\left[\mathbf{n} \cdot \left(-p\mathbf{I} + \mu(\nabla\mathbf{u} + (\nabla\mathbf{u})^T) \right) \cdot \mathbf{n} \right] = \sigma\kappa, \quad (18)$$

where $[\]$ indicates the jump at the interface, i.e., $f_L^I - f_G^I$ for a variable f with superscript I denotes interface, \mathbf{n} is the unit vector normal to the interface, σ is the coefficient of surface tension, and κ is the local curvature of the interface. Notice that with a continuous viscosity and velocity field, the stress jump condition Eq. (18) reduces to

$$[p] = p_L^I - p_G^I = -\sigma\kappa. \quad (19)$$

D. Numerical Methods and High Performance Computing

The flow equations are discretized on a staggered Cartesian grid with the convection terms approximated by a third-order QUICK scheme¹³ and other terms by the standard second-order central difference scheme. A semi-implicit time-advancement scheme is adopted to integrate the momentum equations with the second-order Crank-Nicolson scheme for the diagonal viscous terms and the second-order Adams-Bashforth scheme for the convective terms and other viscous terms. A four-step fractional-step method is employed for velocity-pressure coupling. The pressure Poisson equation is solved using a semi-coarsening multigrid Poisson solver from the HYPRE library from Lawrence Livermore National Laboratory.¹⁴ Details of the numerical methods can be found in the study by Yang and Stern.⁶

The code is parallelized via a domain decomposition (in three directions) technique using the MPI library. All inter-processor communications for ghost cell information exchange are in non-blocking mode. In general, optimal load balance can be achieved except for a small amount of overhead due to interface, which may be unevenly distributed over processors. Parallel I/O using MPI2 have been implemented such that all processors read from and write to one single file simultaneously, which is much more effective than one or a few processors receive data from all processors and write to one or a few files and more convenient than every processor writes its own data files.

III. Results

A. Computational Setup

The simulations are carried out on a two dimensional (2D) computational domain with the boundary conditions specified as shown in Figure 1 for both the wet case (without air injection) and the ALDR case. The air injection geometry, slot A, used in Test 1 in the experiments by Elbing et al.³ is chosen in the ALDR tests. A non-uniform grid of 256×1024 is used first with the streamwise grid refined near the air injector and the grid in the normal direction refined near the wall as shown in Figure 2. This initial coarse grid is designed to resolve the boundary layer, streamwise resolutions are not enough for the water/air interface changes. A wet case without air injection at a Reynolds number of $Re = 2.1 \times 10^8$ is conducted first in order to validate the SA turbulent model with the wall function approach. The computational result is shown in Fig. 3 along with the EFD (experimental fluid dynamics) and analytical solutions. As shown in the figure, the computational result matches the power-law fit very well. As compared to the experimental data, the skin friction coefficient is under predicted. This might be due to grid design and deficiency of SA model, further investigations using finer grid and more advanced turbulence models will be considered in the future work.

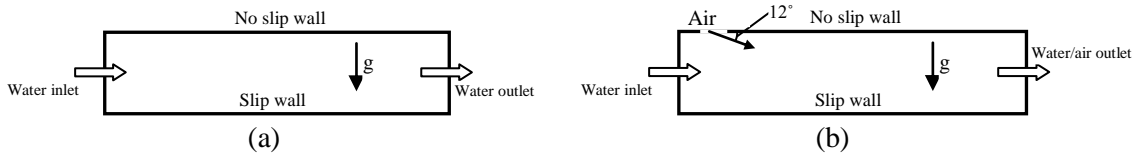


Figure 1. Boundary conditions for wet plate and ALDR simulations.

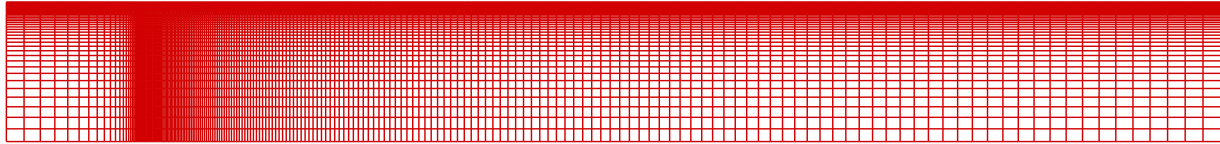


Figure 2. Grid structure of the computational domain for the ALDR.

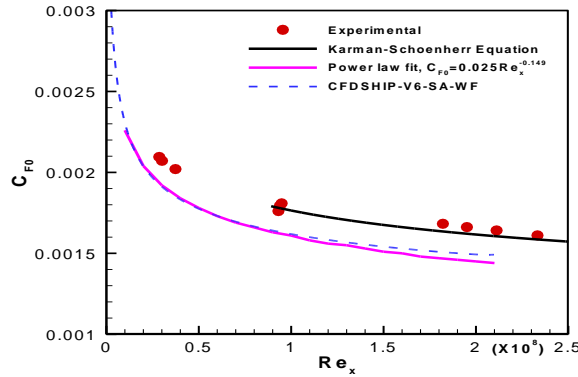


Figure 3. Skin friction coefficient of the wet case as a function of Reynolds number (based on downstream distance).

B. Air Layer Drag Reduction

In the present study, all the simulations are conducted with a Reynolds number of $Re = 7.37 \times 10^7$ which corresponds to Test 1 in Elbing et al. (2008) with a free stream velocity of 6.7 m/s. The largest air flow rate of 15.3 m³/min is used first; later several low air flow rates are employed to investigate the effect on the formation of BDR and ALDR. The simulation matrix is given in Table 1.

Table 1 Simulation Matrix

Injection geometry	Re _{water} (U _∞)	Turbulence model	Grid	Volumetric gas injection rates (Q*)	Flow type and status
Slot A	7.37×10 ⁷ (6.7 m/s)	SA-WF	1024×256	0.5184	ALDR, completed
				0.0864	
				0.0432	
				0.0406	Transitional, completed
				0.0398	
				0.0389	BDR, completed
				0.0345	
				0.0259	
				0.0086	ALDR, completed
				2048×256	
16384×256	0.0864	ALDR, completed			

Note: $Q^* = Q_a / (U_\infty \cdot A_{inj})$

The drag reduction along the plate with an air flow rate of 15.3 m³/min is shown in Fig. 4 where drag reduction of nearly 100% is achieved over the entire plate, which matches the EFD data very well. As shown in Fig. 5, the air layer is formed along the whole length of the plate. It should be noted that at the early stage of the computations water spots are found on the plate and gradually were swept to downstream with the incoming flow. The air flow rate is then reduced to 2.55 m³/min (the lowest in Test 1 of Ref. 3) where a thinner air layer is achieved with the drag reduction approximately 100%. As discussed in Ref. 3, the increase of air flow rate does not apparently increase the drag reduction when air layer is formed. The velocity vector fields with the interface profile overlapped at two different locations along the plate are plotted in Fig. 6. Near the air injector, velocity changes sharply across the interface, whereas in the downstream velocity field across the interface is smooth.

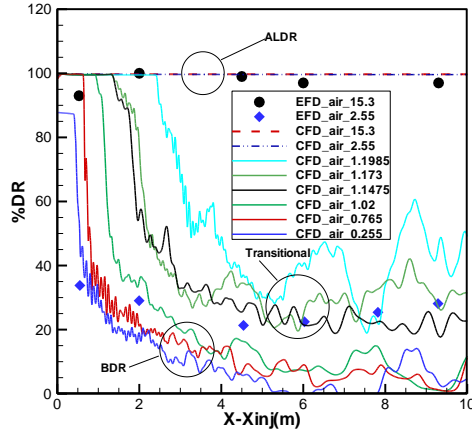


Figure 4. %DR versus $X-X_{inj}$ with different air flow rates Q_a . $U_\infty=6.7$ m/s.

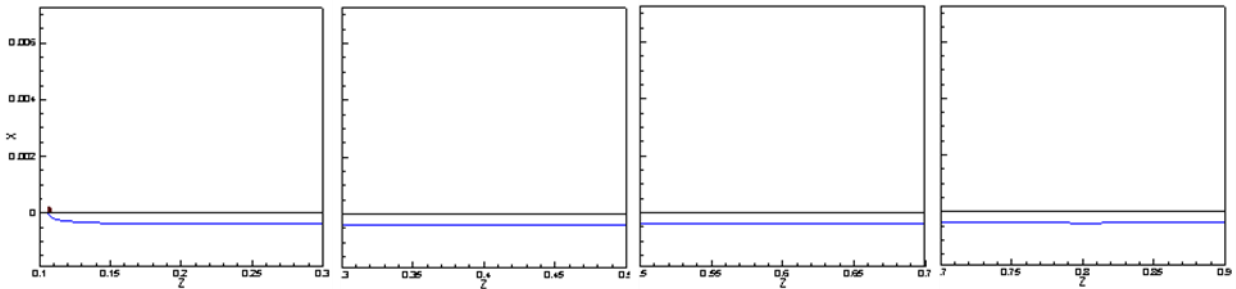


Figure 5. Air layer profile along the plate. $U_\infty=6.7$ m/s, $Q_a=15.3$ m³/min.

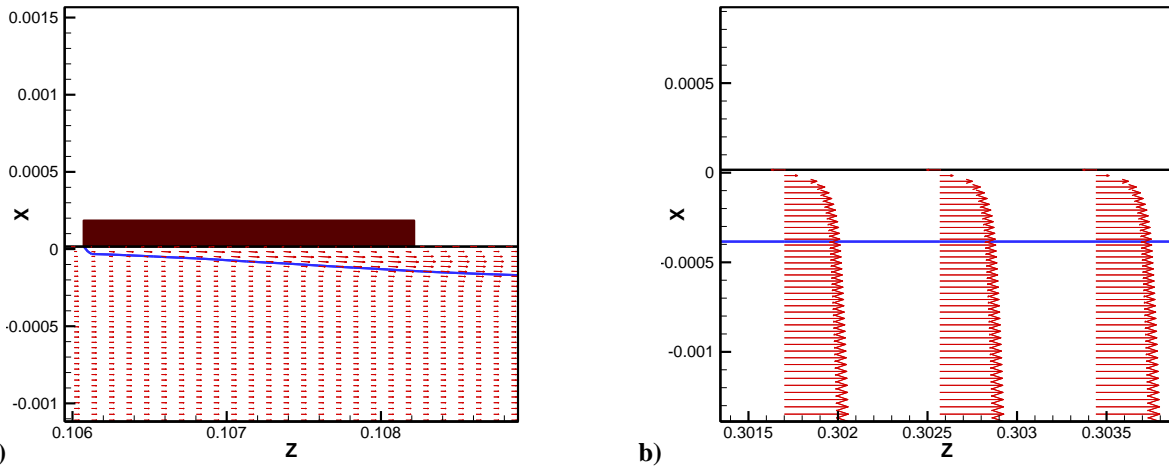


Figure 6. Velocity vector fields along the plate. a) Near the air injector; b) In the middle of plate. $U_\infty=6.7$ m/s, $Q_a=15.3$ m³/min.

In order to investigate the effect of air flow rate on the formation of the ALDR, the air flow rate is then further reduced to a quite small value of 0.255 m³/min. Then the air flow rate is gradually increased to 0.765, 1.02 and 1.1475 m³/min later. As shown in Fig. 4, bubble drag reduction is obtained when the air flow rate is decreased to 0.255, 0.765, 1.02 m³/min. For each case, high levels of drag reduction are achieved only near the air injector and then decay rapidly with downstream distance. Figure 4 also indicates that the increase of air flow rate apparently increases %DR near the air injector and its effect becomes insignificant with downstream distance. This agrees with the BDR features observed in the experiments. As the air flow rate reaches 1.1475 m³/min, apparent %DR increase is achieved along the entire plate, which is close to the transitional region obtained in the experiment with an air flow rate of 2.55 m³/min. It should be noted that the threshold air flow rate necessary to form ALDR is smaller in the present simulation than in the experiments. This deviation from the experiment is probably due to the compressed air injection used in the experiment which is difficult to model in the present study. The grid

resolutions, surface roughness, in flow conditions and surface tension effect are also possible reasons, which will be investigated in the future work. The interface profiles along the plate for BDR, transitional, and ALDR are shown in Fig. 7. The predicted bubble size is almost one order of magnitude larger than the EFD results. %DR versus air flow rate plot at $x = 6$ to 7 m is shown in Fig. 8. BDR is observed over the lower-range of air injection rates, where %DR decreases with downstream distance. The transitional region shows a Rapid %DR increase with air flow rates in most sections of the plate. For the ALDR, high %DR is obtained with no apparent decay with downstream distance over the entire plate. The experimental results indicate that the critical air flow rate increases with Reynolds number.

Since the initial coarse grid is designed for the boundary layer and not enough to resolve the interface changes, the streamwise grid is refined to 2048 and 163824, respectively. The air flow rate is $2.55 \text{ m}^3/\text{min}$ (transitional region in Test 1 of Ref. 3). Although interface instabilities are observed on the refined grids, %DR is still more than 90% as shown in Fig. 8. Grid refinement in the wall normal direction might be needed to further resolve the interface instability. Another very possible reason is due to the two-phase interfacial turbulence modeling. In the present study, the single-phase based RANS equations have been used. The effect of turbulence on the interface and the interface induced turbulence are not considered. For example, the eddy viscosity is found to be over-predicted near the interface in RANS (similarly for LES see the work by Liovic and Lakehal¹⁵). As a result, the small deformations of the interface are smeared out. This problem is especially serious when the interface motion owing much to the turbulence induced disturbances. As demonstrated in a plane water jet test by Shirani et al.¹⁶ using a single-phase based RANS model, the jet does not spread but keeps a uniform cross section throughout the entire jet length. A similar problem is encountered here, the interface does not break up into bubbles but remains a smooth air layer at low air flow rates. As a result of Reynolds-averaging process (or filtering for LES) of RANS, some additional terms should emerge in the momentum and interface advection equations. Hong and Walker¹⁷ have developed a set of Reynolds-averaged equations for the two-phase interfacial flows. However, these equations do not represent a closed system of equations and no model is introduced. Shirani et al.¹⁶ developed a model to include the interface effects in the standard RANS models, and a model for the correlation of the mean fluctuations of VOF with velocity. These models have been applied for the simulation of a plane water jet, very promising results are obtained. This model will be implemented in the future work. It should be noted that it is the first attempt for the two-phase interfacial turbulence modeling considering the interactions of the interface and turbulence. Further tests are required to determine the coefficients of models and derive more sophisticated models.

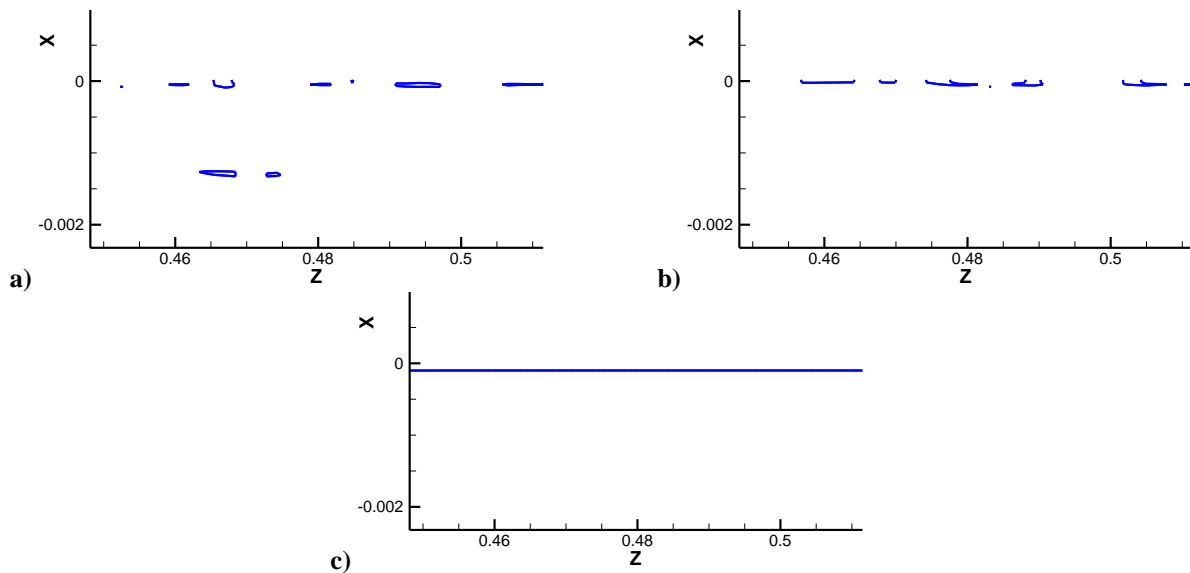


Figure 7. Interface profile along the plate with various air flow rates (magnified view at the middle part), $U_\infty=6.7 \text{ m/s}$. a) BDR ($Q_a=1.02 \text{ m}^3/\text{min}$), bubble size: 0.48 to 4.5 mm; b) Transitional ($Q_a=1.20 \text{ m}^3/\text{min}$); c) ALDR ($Q_a=2.55 \text{ m}^3/\text{min}$).

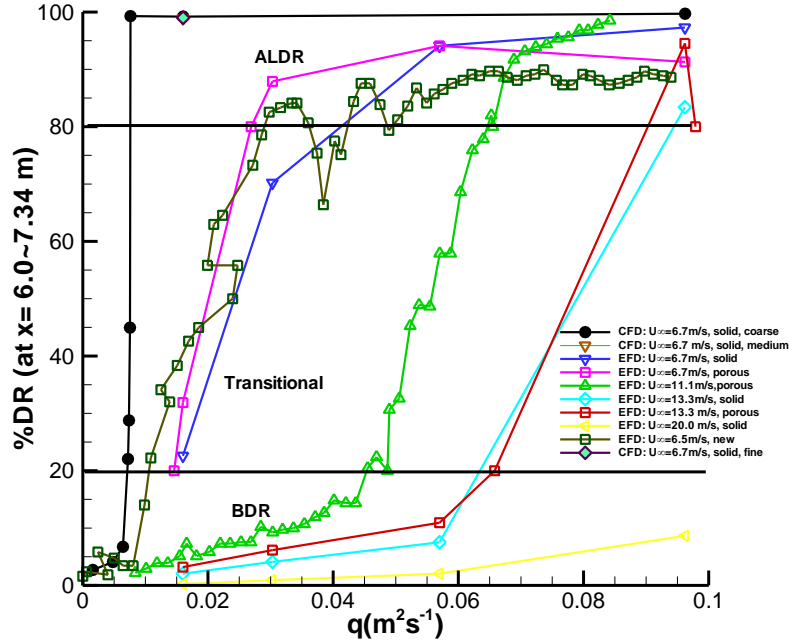


Figure 8. %DR versus air flow rate plot.

IV. Summary and Future Work

The air layer formation in a high Reynolds-number flat plate turbulent boundary layer is simulated using a two-phase URANS solver. The air layer along the entire test plate is successfully achieved and the drag reduction is approximately 100%, which agrees with the experimental findings very well. With reduced air flow rate, BDR is also observed; the computational results also qualitatively match the experiments. The transitional region from BDR to ALDR is also observed in the present simulation. However, the critical air flow rate to form the ALDR is lower in the simulations than in the experiments. Several possible reasons are likely accounting for the low critical air flow rate in the simulations, such as SA-WF turbulence model, three-dimensional instability and surface tension effects. The critical air flow rate does not change much with grid refinement.

In the future work, the computational results will be further verified and validated. The low air flow rate issue will be investigated. The RANS model in the framework of two-equation k -epsilon model proposed by Shirani et al.¹⁶ will be implemented and evaluated in order to account for the interactions between the interface and turbulence. Advanced turbulence models, such as SST Two-Equation model, hybrid RANS/LES, will be considered. Three dimensional LES simulations at relatively low Reynolds numbers will also be conducted. Three-dimensional instability and surface tension effect will be investigated. The mechanism of the formation of the ALDR, transitional region and BDR, flow structure, and interface instability, will be analyzed in the future work.

Acknowledgments

The Office of Naval Research under Grant N00014-08-1-0620, administered by Dr. Patrick Purtell, sponsored this research under the project "Two-Phase URANS/DES Simulations of Large Scale/RE Air Layer Drag Reduction". The simulations were performed using DoD HPC resources.

References

- ¹Merkle, C., and Deutsch, S., "Microbubble Drag Reduction in Liquid Turbulent Boundary Layers," *Appl. Mech. Rev.*, Vol. 45, No. 3, 1992, pp. 103-127.
- ²Sanders, W.C., Winkel, E.S., Dowling, D.R., Perlin, M., and Ceccio, S.L., "Bubble Friction Drag Reduction in a High-Reynolds-Number Flat-Plate Turbulent Boundary Layer," *J. Fluid Mech.*, Vol 552, 2006, pp. 353-380.
- ³Elbing, B.R., Winkel, E.S., Lay, K.A., Ceccio, S.L., Dowling, D.R., and Perlin, M., "Bubble-Induced Skin-Friction Drag Reduction and the Abrupt Transition to Air-Layer Drag Reduction," *J. Fluid Mech.*, Vol. 612, 2008, pp. 201-236.
- ⁴Ceccio, S.L., "Evaluation of Air Cavity Lubrication at High Reynolds Numbers," *Air Layer Drag Reduction Program Review Meeting*, Stanford University, Stanford, California, September 15, 2009.
- ⁵Amromin, E., and Mizine, I., "Partial Cavitation as Drag Reduction Technique and Problem of Active Flow Control," *Marine Technology*, Vol. 40, 2003, pp. 181-188.

- ⁶Yang, J., and Stern, F., "Sharp Interface Immersed-Boundary/Level-Set Method for Wave-Body Interactions," *Journal of Computational Physics*, Vol. 228, 2009, pp. 6590-6616.
- ⁷Wang, Z., Yang, J., Koo, B., and Stern, F., "A Coupled Level Set and Volume-of-Fluid Method for Sharp Interface Simulation of Plunging Breaking Waves," *International Journal of Multiphase Flow*, Vol. 35, 2009, pp. 227-246.
- ⁸Bhushan, S., Carrica, P.M., Yang, J., and Stern, F., "Scalability Study and Large Grid Computations for Surface Combatant Using CFDship-Iowa," *International Journal of High Performance Computing*, 2010 (under revision).
- ⁹Spalart, P. R., and Allmaras, S. R., "A One-Equation Turbulence Model for Aerodynamic Flows," *AIAA-Paper 92-0439*, No. 1, 1992, pp. 5-21.
- ¹⁰Mariani-D, J., Zilliac, G. G., Chow, J. S., and Bradshaw, P., "Numerical/Experimental Study of a Wingtip Vortex in the Near Field," *AIAA Journal*, Vol. 33, No. 9, 1995, pp. 1561-1568.
- ¹¹Shih, T. H., Povinelli, L.A., and Liu, N. S., "Application of Generalized Wall Function for Complex Turbulent Flows," *Journal of Turbulence*, Vol. 4, 2003, pp. 1-16.
- ¹²Sussman, M., Smereka, P., and Osher, S., "A level set approach for computing solutions to incompressible two-phase flow," *Journal of Computational Physics*, Vol. 114, 1994, pp. 146-159.
- ¹³Leonard, B.P., "A stable and accurate modeling procedure based on quadratic interpolation", *Comput. Methods Appl. Mech. Engrg.*, Vol. 19, 1979, pp. 58-98.
- ¹⁴Falgout, R.D., Jones, J.E., and Yang, U.M., "The Design and Implementation of HYPRE, a Library of Parallel High Performance Preconditioners," *Numerical Solution of Partial Differential Equations on Parallel Computers*, A.M. Bruaset and A. Tveito, eds., Springer-Verlag, Vol. 51, 2006, pp. 267-294.
- ¹⁵Liovic, P., and Lakehal, D., "Multi-Physics Treatment in the Vicinity of Arbitrarily Deformable Gas-Liquid Interfaces," *Journal of Computational Physics*, Vol. 222, 2007, pp. 504-535.
- ¹⁶Shirani E, Jafari A, and Ashgriz N, "Turbulence Models for Flows with Free Surfaces and Interfaces," *AIAA Journal*, Vol. 44, No. 7, 2006, pp. 1454-1462.
- ¹⁷Hong, W.L., and D.T. Walker, D.T., "Reynolds-Averaged Equations for Free-Surface Flows with Application to High-Froude-Number Jet Spreading," *J. Fluid Mech.*, Vol. 417, 2000, pp. 183-209.